International Journal of Multiphase Flow 132 (2020) 103398

Contents lists available at ScienceDirect

International Journal of Multiphase Flow

journal homepage: www.elsevier.com/locate/ijmulflow

Theoretical model of a finite force at the moving contact line

Peter Zhang [a], Kamran Mohseni [a,b,*]

[a] Department of Mechanical and Aerospace Engineering, University of Florida, Gainesville, FL. United States
[b] Department of Electrical and Computer Engineering, University of Florida, Gainesville, FL. United States

ARTICLE INFO

Article history:
Received 17 November 2018
Revised 28 March 2020
Accepted 10 June 2020
Available online 18 July 2020

Keywords:
Moving contact line
Dynamic contact angle
Multiphase flows

ABSTRACT

In theoretical analyses of the moving contact line, an infinite force along the solid wall has been reported based off the non-integrable stress along a *single* interface. In this investigation we demonstrate that the stress singularity is integrable and results in a *finite* force at the moving contact line if the contact line is treated as a one-dimensional manifold and all *three* interfaces that make up the moving contact line are taken into consideration. This is due to the dipole nature of the vorticity and pressure distribution around the moving contact line. Mathematically, this finite force is determined by summing all the forces that act over an infinitesimally small cylindrical control volume that encloses the entire moving contact line. With this finite force, we propose a new dynamic Young's equation for microscopic dynamic contact angle that is a function of known parameters only, specifically the interface velocity, surface tension, and fluid viscosity. We combine our model with Cox's model for apparent dynamic contact angle and find good agreement with published dynamic contact angle measurements.

1. Introduction

The moving contact line (MCL) is a unique and challenging problem that influences many natural and industrial processes such as drop impact (Yarin, 2006), boiling (Dhir, 1998), industrial coatings (Weinstein and Ruschak, 2004), and inkjet printing (Derby, 2010), among others. Some of the aspects that make the MCL such a complex problem include its multiscale nature (Snoeijer and Andreotti, 2013), the apparent breakdown of the no-slip assumption (Dussan, 1976), hysteresis (Eral, Oh, et al., 2013), and dependence on surface properties (Quéré, 2008). In recent years industrial and medical applications have spurred MCL research towards even more challenging problems such as wetting failure (de Gennes, 1985; Landau and Levich, 1988), air entrainment (Vandre, Carvalho, Kumar, 2014), electrowetting (Mugele and Baret, 2005), and phase change at the contact line (Gelderblom et al., 2012, 2013). While these problems are important for advancing multiphase technology, there is still no consensus on the physics that govern contact line movement over a smooth surface (Blake, 2006; Bonn et al., 2009; Snoeijer and Andreotti, 2013; Sui et al., 2014). Understanding the MCL dynamics over a smooth surface is essential to developing models for more complex wetting phenomena and thus it has remained a topic of significant interest for several decades.

Two early investigations of this fundamental problem were conducted by Moffatt (1964) and Huh and Scriven (1971). In these works, the MCL geometry was modeled by three planar interfaces intersecting with a contact angle ϕ and characterized by an interface velocity U, as shown in Fig. 1. Moffatt examined a viscous fluid displacing an inviscid gas and reported a solution with an "infinite stress and pressure (both of order r^{-1}) on the plate at the corner". Huh & Scriven extended this analysis to two viscous fluids and reported that "the total force exerted on the solid surface is logarithmically infinite" due to the singular stress at the MCL. These investigations, among others (Blake, 2006; Bonn et al., 2009; Cox, 1986; de Gennes, 1985; Eggers and Stone, 2004; Hocking, 1977; Shikhmurzaev, 1997; Snoeijer and Andreotti, 2013; Sui et al., 2014), have concluded that the hydrodynamic solution does not accurately model the MCL because an infinite force is not physical and this result has come to be known as the MCL problem, or "Huh & Scriven's paradox" (Bonn et al., 2009).

Since these early works, several MCL theories have been developed and include the molecular kinetic theory (MKT) (Blake and Haynes, 1969), interface formation theory (IFT) (Shikhmurzaev, 1997, 2007), and hydrodynamic theory (Cox, 1986; Dussan, 1976; Voinov, 1976) among others (Petrov and Petrov, 1992; Pismen, 2002; Seppecher, 1996). In many of these models, microscopic physical mechanisms relieve the stress singularity and allows the interface to move relative to the solid without inducing a singular

* Corresponding author.
E-mail address: mohseni@ufl.edu (K. Mohseni).
URL: http://www.enstrophy.mae.ufl.edu (K. Mohseni)

https://doi.org/10.1016/j.ijmultiphaseflow.2020.103398
0301-9322/

force. MKT describes the motion of the contact line as a molecular process where molecules attach and detach from the solid surface with some characteristic frequency and displacement. The rate at which these molecules are displaced induces changes in the local surface tension which subsequently affects the dynamic contact angle. Typically the length scale of the molecular displacement is on the order of nanometers while the frequency of this displacement is inversely proportional to the viscosity of the fluid. Through experiment the molecular frequency and displacement have been determined for specific fluid-solid pairs however, it is often difficult to predict these parameters for general cases (Blake, 2006).

Interface formation theory is built on the premise that near a MCL, fluid elements move from one interface to another in finite time so that the fluid exhibits a rolling type motion rather than a sliding type motion associated with fluid slip. As fluid elements transition from one interface to another, IFT posits that the fluid properties will gradually change such that a surface tension gradient will be generated near the MCL. Shikhmurzaev (1997) proposes an equation of state to relate the surface tension to the interfacial density multiplied by a phenomenological coefficient. Assuming that the Young's equation is valid for dynamic contact lines, the predicted surface tension gradient results in a change in contact angle. Proponents of IFT report that the model contains no singularities, preserves the rolling kinematics of MCLs, and captures the effects of the local flow field on the dynamic contact angle (Shikhmurzaev, 2006). Based on these characteristics, and the possibility of simulating high Capillary number flows without slip, IFT has been praised as a potentially far-reaching approach (Blake, 2006).

The hydrodynamic theory of the MCL is based on classical continuum fluid mechanics but relaxes the no-slip condition. In many cases the Navier-slip boundary condition (Navier, 1823) and a constant slip length is used to determine the flow near the MCL. However, recent molecular dynamics simulations have indicated that the slip length is dependent on the fluid stress (Thompson and Troian, 1997) and that fluid slip near the MCL may require a more generalized slip boundary condition (Thalakkottor and Mohseni, 2016). In general, hydrodynamic models find that the interface shape varies logarithmically with respect to distance from the contact line and is a function of the microscopic contact angle and inner to outer length scale ratio (Cox, 1986; Hocking and Rivers, 1982; Voinov, 1976). In many applications, a constant microscopic contact angle and length scale ratio allows the hydrodynamic model to capture the shape of the interface (Ramé and Garoff, 1996; Sui and Spelt, 2013). However, there is no physical reason why these parameters should be constant and there have been a growing number of publications that have reported that these parameters should vary as a function of contact line velocity (Ramé et al., 2004; Shen and Ruth, 1998; Sheng and Zhou, 1992).

In each of the theories reviewed above, molecular scale physics are used to remove the stress singularity at the MCL. As a consequence, the MCL becomes a multiscale problem that couples macroscopic dynamics to microscopic physical parameters like the molecular equilibrium frequency of MKT, the interfacial density of IFT, or the slip length in hydrodynamic models. Currently these microscopic parameters are difficult to determine theoretically and are most often obtained by fitting the theory to experimental measurements. Through the fitting process, most of these theories have reported agreement with experimental measurements (Blake and Shikhmurzaev, 2002; Cox, 1986; Duvivier et al., 2011; Hoffman, 1975; Katoh et al., 2015; Seveno et al., 2009) and it has been difficult to judge which theory captures the true physics of the contact line. As a result, the physics of the MCL are still debated to this day and the field continues to grow larger and more diverse. For additional information regarding the MCL, we refer the reader to the following references: Blake (2006); Dussan (1979); Bonn et al., 2009; Snoeijer and Andreotti (2013); Sui et al. (2014); de Gennes (1985).

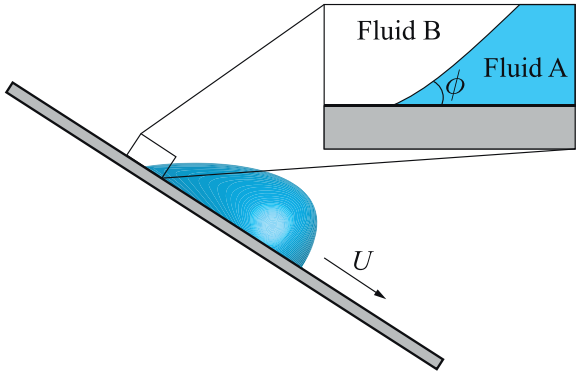

Fig. 1. Schematic of a droplet sliding down an inclined plate. Near the moving contact line, the interface has minimal curvature and intersects the solid with a dynamic contact angle ϕ.

Looking back on the evolution of the MCL problem, it appears that many investigations were motivated by the conclusions of Moffatt and Huh & Scriven who determined that a stress that scales as $1/r$ is not integrable and that the hydrodynamic solution of the MCL subject to the no-slip boundary condition predicts an unphysical infinite force. Interestingly we have observed that a continuum field that scales as $1/r$ is treated as an *integrable* singularity in other fields, and even in continuum fluid flows. In electromagnetism, an electric field that scales as $1/r$ is integrable and correlated to the total charge (Griffiths, 1972). In potential flow theory, a velocity field that scales with $1/r$ is integrable and directly related to the total mass flux of a line source (Batchelor, 1967). Even in Stokes flows, the two-dimensional Stokeslet contains a stress singularity that scales as $1/r$ and is considered an integrable singularity that is correlated to a finite force (Crowdy and Or, 2010). Given these numerous examples of integrable $1/r$ singularities, one begins to wonder why is the MCL different?

Motivated by these observations, this work will revisit the classic hydrodynamic solution and present an alternative perspective of the stress singularity. We will begin with a brief review of the Stokes solution to the MCL problem in §2. In §3, we will show that classical hydrodynamics models the contact line region as a mathematical line, i.e. a one-dimensional manifold. By treating the MCL as a one-dimensional manifold, we find that the total force exerted by the fluid is finite and a function of the surface tension, interface velocity, and fluid viscosity. §4 presents a discussion of this finite force and a comparison with previous works to show that the logarithmically infinite force only arises if the MCL is treated as a two-dimensional manifold. Based on this finite force result, we propose a model for the microscopic dynamic contact angle in §5 and provide supporting experimental comparisons. Similarities between the MCL, Stokeslet, and cusped fluid interface are discussed in §6 as they all exhibit singular stresses and finite forces. Concluding remarks are found in §7.

2. Stokes flow solution to the moving contact line problem

The primary analysis and results of this paper are based off the well-known Stokes solution to the MCL problem originally presented by Cox (1986). To establish a foundation for the following discussion, this section will provide a brief review of Cox's solution. At a top level, Cox's solution to the MCL flow, shown in Fig. 2, is obtained using perturbation theory and expanding about the zeroth order solution in the small Capillary number limit. As shown in the past (Cox, 1986; Snoeijer, 2006), the zeroth order flow corresponds to the boundary driven planar wedge whose so-

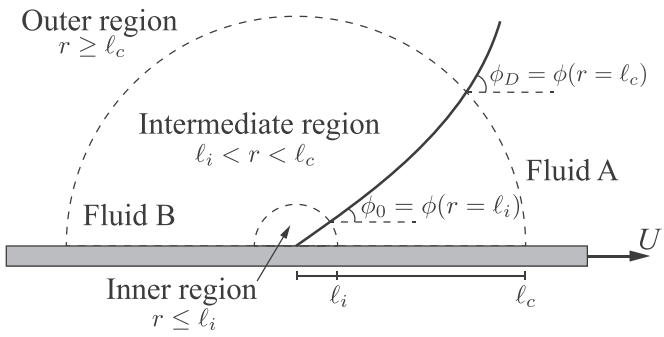

Fig. 2. Geometry of a moving contact line in a cylindrical coordinate system (r, θ) whose origin is fixed at the contact line. In this moving reference frame, the solid boundary moves with a velocity U relative to the fluid-fluid interface whose shape is given by $\phi(r)$. The inner, intermediate, and outer regions follows the definitions by Cox (1986) where ℓ_i and ℓ_c are the inner and outer length scales, respectively. Inside the inner region, Cox showed that the interface is approximately planar in the limit of $Ca \to 0$ and thus ϕ_0 is approximately equal to the contact line angle at the solid surface.

lution is known analytically from the works of Moffatt (1964) and Huh and Scriven (1971) and valid in the intermediate and outer regions where the no-slip condition is valid. From this zeroth order solution, Cox and others have iteratively solved for higher order terms. Below, we present Cox's derivation of the zeroth and first order solution.

The analysis performed by Cox begins with assuming that the Reynolds number is significantly smaller than one ($Re = \rho \ell U/\mu \ll 1$) so that the dynamics of fluids A and B near the MCL are governed by the Stokes and continuity equations given by

$$\nabla^2 \boldsymbol{u}_A^* = \nabla p_A^*, \qquad \nabla \cdot \boldsymbol{u}_A^* = 0, \tag{1}$$

$$\lambda \nabla^2 \boldsymbol{u}_B^* = \nabla p_B^*, \qquad \nabla \cdot \boldsymbol{u}_B^* = 0. \tag{2}$$

ρ denotes the density, ℓ the characteristic length scale, U the interface velocity, μ the viscosity, $\lambda = \mu_B/\mu_A$ the viscosity ratio, $\boldsymbol{u}^*$ the dimensionless velocity, and p^* the dimensionless pressure. If fluid A or B is not specified in the subscript, then the variable is representative of either fluid. In this MCL problem, the fluid is subject to the no-slip and zero penetration boundary condition along all interfaces in addition to the continuity of tangential stress and balance of normal stress at the fluid-fluid interface. In order to make the problem tractable, Cox assumed that Capillary number is significantly smaller than one ($Ca = \mu U/\sigma \ll 1$) and expanded the velocity, pressure, and fluid-fluid interface shape as

$$\boldsymbol{u}^* = \boldsymbol{u}_0^* + Ca\boldsymbol{u}_1^* + \dots, \tag{3}$$

$$p^* = p_0^* + Cap_1^* + \dots, \tag{4}$$

$$\phi = \phi_0 + Ca\phi_1 + \dots. \tag{5}$$

Here, σ denotes the surface tension. Given the expansions above, other quantities of interest such as the stress tensor, $\boldsymbol{T}$, or interface curvature, κ, can be written using similar expansions. Substituting equations (3)-(4) into equation (1)-(2) and collecting terms of order Ca^0 yields the zeroth order governing equations which are given by

$$\nabla^2 \boldsymbol{u}_{A0}^* = \nabla p_{A0}^*, \qquad \nabla \cdot \boldsymbol{u}_{A0}^* = 0, \tag{6}$$

$$\lambda \nabla^2 \boldsymbol{u}_{B0}^* = \nabla p_{B0}^*, \qquad \nabla \cdot \boldsymbol{u}_{B0}^* = 0. \tag{7}$$

As noted by Cox, Capillary number only appears in the normal stress boundary condition at the fluid-fluid interface, i.e.

$$Ca\hat{\boldsymbol{n}} \cdot [\![\boldsymbol{T}_0 + Ca\boldsymbol{T}_1 + \dots]\!] \cdot \hat{\boldsymbol{n}}' = \kappa_0 + Ca\kappa_1 + \dots, \tag{8}$$

where $[\![\cdot]\!]$ denotes the jump of a quantity across an interface whose normal vector is denoted by $\hat{\boldsymbol{n}}'$. Collecting terms of order Ca^0, one obtains $\kappa_0 = 0$ so that the zeroth order solution is the flow in a planar wedge with angle ϕ_0. To obtain the zeroth order solution, Cox rewrites the Stokes equation as the biharmonic stream function equation, $\nabla^4 \psi = 0$, whose general solution is known and given in Appendix A. Applying the aforementioned boundary conditions, Cox identifies the zeroth order stream function as

$$\psi_0 = rU[A\cos(\theta) + B\sin(\theta) + C\theta\cos(\theta) + D\theta\sin(\theta)], \tag{9}$$

where (r, θ) is the local cylindrical coordinate system. This stream function solution represents the flow in the intermediate region, see equations (6.7) and (7.8) from Cox (1986). The coefficients A, B, C, and D are analytically known and presented in Appendix B, in addition to the zeroth order velocity, pressure, and vorticity. The normal stress jump that appears in the zeroth order solution, i.e.

$$-(r/\ell)^{-1} m(\phi_0, \lambda) = -\frac{2}{r/\ell}[\lambda(C_B\cos\phi_0 + D_B\sin\phi_0) - (C_A\cos\phi_0 + D_A\sin\phi_0)], \tag{10}$$

is accounted for by the curvature of the first order interface shape, that is

$$\frac{\partial \phi_1}{\partial r} = (r/\ell)^{-1} m(\phi_0, \lambda). \tag{11}$$

Integrating the equation above yields $\phi_1 = m(\phi_0, \lambda)\ln(r/\ell) + Q$ and the interface shape

$$\phi = \phi_0 + Ca[m(\phi_0, \lambda)\ln(r/\ell) + Q] + \dots, \tag{12}$$

where Q is an unspecified constant of integration. The equation above is the widely recognized general form of the fluid-fluid interface under steady motion (Cox, 1986; Sibley et al., 2015). In the paper by Cox, higher order terms were not reported as they had a negligible effect. In the next section, we revisit this classic solution to the MCL flow and demonstrate that the singular stress of the dominant zeroth order solution exerts a finite force at the moving contact line.

3. Forces acting at the contact line

In the past, moving contact line analyses have often utilized integral equations that were derived for fluid interfaces. However, the moving contact *line* is a one-dimensional manifold unlike fluid interfaces, which are two-dimensional manifolds. A fluid interface is uniquely defined by a single normal vector while a contact line has multiple normal vectors. This multivaluedness subsequently appears in the hydrodynamic solution which exhibits a multivalued velocity, stress, vorticity, and pressure along the contact line. In light of these contact line attributes, let us take a step back and consider a summation of forces acting on a finite sized cylindrical control volume, V, with radius ϵ centered around the contact line, as shown in Fig. 3. This volume is bounded by the surface $\mathcal{S}$ and intersects the interfacial surfaces denoted by $\mathcal{I}$. As we will demonstrate later, this is the control volume necessary to derive the Young's equation and is the one-dimensional analogue to the rectangular control volume used to derive the balance of forces on a fluid interface which is a two-dimensional manifold. For a steady problem, the sum of all the forces acting on the control volume V is given by

$$\Sigma \boldsymbol{f} = \underbrace{\iint_{\mathcal{S}} \hat{\boldsymbol{n}} \cdot \boldsymbol{T} dA}_{\text{surface force}} + \underbrace{\iiint_{V} \rho \boldsymbol{g} dV}_{\text{body force}} + \underbrace{\iint_{\mathcal{I}} \nabla_\pi \cdot \boldsymbol{T}_\pi dA}_{\text{surface tension gradient}} + \underbrace{\int_{\mathcal{L}} [\![\boldsymbol{T}_\pi \cdot \hat{\boldsymbol{t}}']\!] ds}_{\text{surface tension force}} = 0, \tag{13}$$

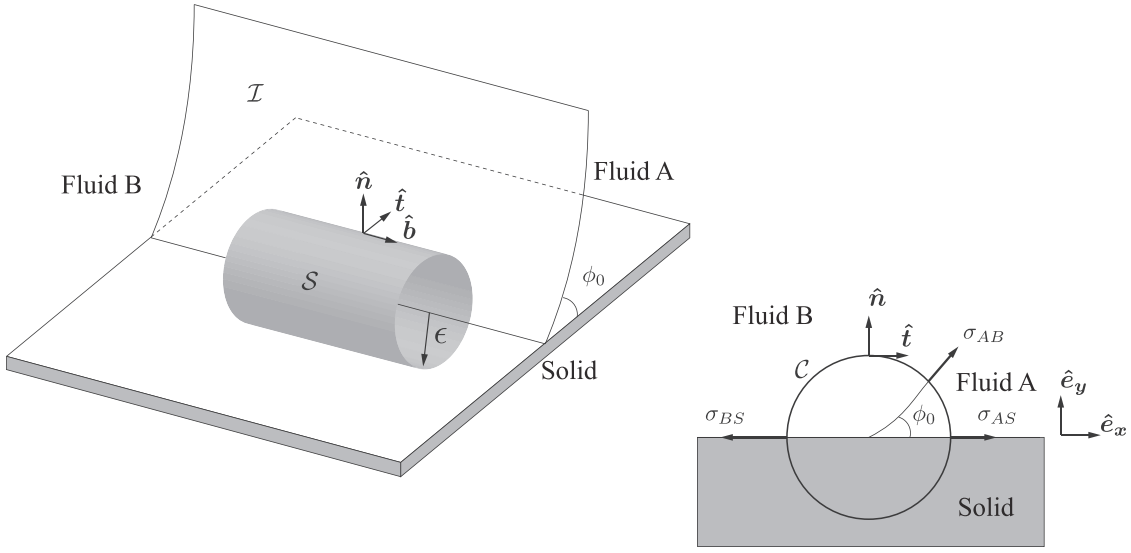

Fig. 3. Schematic of the cylindrical control volume V with radius ϵ that is bounded by the surface S and centered at the MCL. The moving contact line has a contact angle of ϕ_0. $\hat{\boldsymbol{n}}$ and $\hat{\boldsymbol{t}}$ denote the unit normal and tangential vectors of the contour $\mathcal{C}$. $\mathcal{I}$ denotes the interfacial surfaces and σ denotes the surface tension force between fluid A, B, and the solid.

assuming massless interfaces (Slattery, Sagis, Oh, 2007). $\boldsymbol{g}$ denotes the body force, the subscript π denotes surface quantities, *CL* denotes the contact line, and $\hat{\boldsymbol{t}}'$ denotes the unit tangential vectors of the interfaces. In the limit as $\epsilon \to \ell_i$, where ℓ_i denotes the distance from the contact line over which fluid slip occurs, the equation above represents the sum of all forces acting over the MCL region. Note that the last term of Eq. 13 should be interpreted as the surface tension force acting on the control volume at $r = \epsilon$ and *CL* indicates that the force is integrated in the binormal direction (into/out of the page) and parallel to the contact line. In some works ℓ_i is sometimes denoted by the slip length, ℓ_s, because they are often considered to be the same order of magnitude. However they are not equivalent and ℓ_i and ℓ_s are treated as separate length scales in this work. For this analysis, we will assume that there are zero body forces ($\boldsymbol{g} = 0$) and zero surface tension gradients ($\nabla_\pi \cdot \boldsymbol{T}_\pi = 0$). As a result, the x and y component of the forces (per unit contact line length) acting on the control volume are reduced to

$$\Sigma f_x = \lim_{\epsilon \to \ell_i} \oint_{\mathcal{C}} \hat{\boldsymbol{n}} \cdot \boldsymbol{T} \cdot \hat{\boldsymbol{e}}_{\boldsymbol{x}} ds + \sigma_{AS} - \sigma_{BS} + \sigma_{AB}\cos(\phi_0) = 0, \tag{14}$$

$$\Sigma f_y = \lim_{\epsilon \to \ell_i} \oint_{\mathcal{C}} \hat{\boldsymbol{n}} \cdot \boldsymbol{T} \cdot \hat{\boldsymbol{e}}_{\boldsymbol{y}} ds + \sigma_{AB}\sin(\phi_0) = 0, \tag{15}$$

where $\mathcal{C}$ denotes the contour path. The effects of surface tension gradients are considered in a related work by Thalakkottor and Mohseni (2019).

For the forces acting in the x direction, we decompose the stress integral into three segments that lie inside each material so that the integral above is rewritten as

$$\begin{aligned}\Sigma f_x = &\lim_{\epsilon \to \ell_i} \int_0^{\phi_0} \hat{\boldsymbol{e}}_{\boldsymbol{r}} \cdot (\boldsymbol{T}_{A0} + Ca\boldsymbol{T}_{A1} + \dots) \cdot \hat{\boldsymbol{e}}_{\boldsymbol{x}} r d\theta \\ &+ \lim_{\epsilon \to \ell_i} \int_{\phi_0}^{\pi} \hat{\boldsymbol{e}}_{\boldsymbol{r}} \cdot (\boldsymbol{T}_{B0} + Ca\boldsymbol{T}_{B1} + \dots) \cdot \hat{\boldsymbol{e}}_{\boldsymbol{x}} r d\theta \\ &+ \lim_{\epsilon \to \ell_i} \int_{\pi}^{2\pi} \hat{\boldsymbol{e}}_{\boldsymbol{r}} \cdot \boldsymbol{T}_S \cdot \hat{\boldsymbol{e}}_{\boldsymbol{x}} r d\theta + \sigma_{AS} - \sigma_{BS} + \sigma_{AB}\cos(\phi_0) = 0.\end{aligned} \tag{16}$$

Here, the integral of $\boldsymbol{T}_S$ represents the force induced by the stress of the enclosed solid, $\boldsymbol{f}_S$. To evaluate the fluid stress tensor integrals, we begin with the zeroth order solution and use the stress tensor decomposition $\boldsymbol{T} = \hat{\boldsymbol{T}} - 2\mu\boldsymbol{B}$, where $\hat{\boldsymbol{T}} = -p\boldsymbol{I} + 2\mu\boldsymbol{\Omega}$ is the reduced stress tensor, $\boldsymbol{\Omega}$ is the vorticity tensor, and $\boldsymbol{B} = (\nabla \cdot \boldsymbol{u})\boldsymbol{I} - (\nabla \boldsymbol{u})^T$ is the surface deformation rate tensor. With this decomposition, the first stress tensor integral in equation (16) is rewritten as

$$\int_0^{\phi_0} \hat{\boldsymbol{e}}_{\boldsymbol{r}} \cdot \boldsymbol{T}_{A0} \cdot \hat{\boldsymbol{e}}_{\boldsymbol{x}} r d\theta = \int_0^{\phi_0} \hat{\boldsymbol{e}}_{\boldsymbol{r}} \cdot \hat{\boldsymbol{T}}_{A0} \cdot \hat{\boldsymbol{e}}_{\boldsymbol{x}} r d\theta - 2\mu_A \int_0^{\phi_0} \hat{\boldsymbol{e}}_{\boldsymbol{r}} \cdot \boldsymbol{B}_{A0} \cdot \hat{\boldsymbol{e}}_{\boldsymbol{x}} r d\theta, \tag{17}$$

for the zeroth order solution. The force contribution of the surface deformation rate tensor is identically zero, as one can show that

$$\hat{\boldsymbol{e}}_{\boldsymbol{r}} \cdot \boldsymbol{B}_{A0} = -\frac{\partial u_{0r}}{\partial r}\hat{\boldsymbol{e}}_{\boldsymbol{r}} - \frac{\partial u_{0\theta}}{\partial r}\hat{\boldsymbol{e}}_{\boldsymbol{\theta}} = 0,$$

since both the radial and azimuthal components of the zeroth order velocity are independent of r. This is consistent with the findings of Wu et al. (2006), who reported that the surface deformation rate tensor does not contribute to the total surface force over a closed boundary if viscosity is constant. By substituting the zeroth order solution for pressure and vorticity into the first term on the right hand side of equation (17), we obtain

$$\begin{aligned} f_{A0,x} &= \lim_{\epsilon \to \ell_i} \int_0^{\phi_0} \hat{\boldsymbol{e}}_{\boldsymbol{r}} \cdot \hat{\boldsymbol{T}}_{A0} \cdot \hat{\boldsymbol{e}}_{\boldsymbol{x}} r d\theta \\ &= \lim_{\epsilon \to \ell_i} \int_0^{\phi_0} (-p_{A0}\hat{\boldsymbol{e}}_{\boldsymbol{r}} + \mu_A \omega_{A0}\hat{\boldsymbol{e}}_{\boldsymbol{\theta}}) \cdot \hat{\boldsymbol{e}}_{\boldsymbol{x}} r d\theta \\ &= -\mu_A U \lim_{\epsilon \to \ell_i} \int_0^{\phi_0} \left\{ \frac{2}{r}[C_A\cos(\theta) + D_A\sin(\theta)]\cos(\theta) \right. \\ &\quad \left. + \frac{2}{r}[C_A\sin(\theta) - D_A\cos(\theta)]\sin(\theta) \right\} r d\theta \\ &= -2\phi_0\mu_A U C_A. \end{aligned}$$

The result above shows that the zeroth order viscous force contribution from fluid A in the x direction ($f_{A0,x}$) is independent of r and a function of contact angle, viscosity, and interface velocity only. The same analysis performed on the segment that lies in fluid B and for the zeroth order fluid stress integrals in the y direction allows us to rewrite equations (14) and (15) as

$$2\phi_0\mu_A U C_A + 2(\pi - \phi_0)\mu_B U C_B - \sigma_{AB}\cos(\phi_0) = \sigma_{AS} - \sigma_{BS} + f_{S,x}, \tag{18}$$

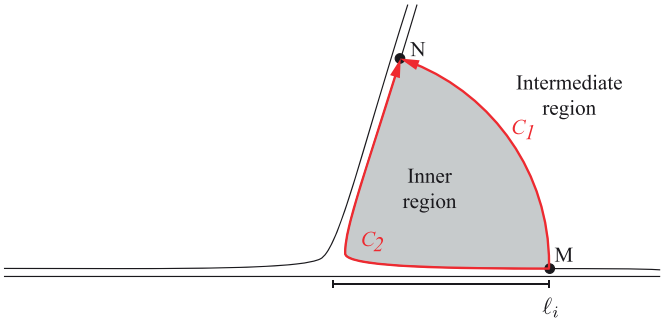

Fig. 4. Fully resolved MCL region. Both the path C_1 and C_2 connect the point M to N, however C_1 lies in the intermediate region where no-slip is valid and C_2 lies inside the inner region where fluid slip is present.

$$2\phi_0\mu_A U D_A + 2(\pi - \phi_0)\mu_B U D_B - \sigma_{AB}\sin(\phi_0) = f_{S,y}, \tag{19}$$

and represents the balance of forces in the x and y direction when the sum of all forces is zero and the moving contact line is steady. The equations above are zeroth order accurate and have been organized so that the left hand side contains the forces that the fluid exerts on the solid, and the right hand side contains the forces that the solid exerts on the fluid.

The finite force of the analysis above captures the total integrated force of the inner slip region ($r < \ell_i$) because the integral of stress in a Stokes flow is independent of path. Specifically, the integral form of the two-dimensional Stokes equation is given by

$$\oint \boldsymbol{T}\cdot\hat{\boldsymbol{n}}ds = 0, \tag{20}$$

which means that the integral of stress is path independent for any boundary condition. Consider the fully resolved contact line depicted in Fig. 4 where the path C_1 lies in the intermediate no-slip region and C_2 lies in the inner slip region. Path independence ensures that the integral of stress along the path C_1 and C_2 are equal so that

$$\int_{C_1} \boldsymbol{T}\cdot\hat{\boldsymbol{n}}ds = \int_{C_2} \boldsymbol{T}\cdot\hat{\boldsymbol{n}}ds. \tag{21}$$

Thus, the total integrated force along the contour $\mathcal{C}$ captures the effect of slip in the inner region without resolving the inner velocity field. This property of path independence allows us to construct a 'sharp line' approximation of the MCL as an extension of the sharp interface approximation of the diffuse interface. In the 'sharp line' limit we model the inner region as a mathematical line ($\ell_i \to 0$) where the total integrated force of the inner slip region (known as the unbalanced Young's force) is preserved by the jump in stress across the contact line. This is a direct extension of the sharp interface approximation where the integral of stress inside a diffuse interface (known as surface tension) is preserved by the jump in stress across the sharp interface. In both the sharp interface and sharp line limit, an integrably singular stress acts on an infinitesimally small area resulting in a finite force.

The analysis above, which has been performed for the zeroth order solution, can also be applied to the first order solution. Given the first order interface shape in equation (12), and assuming that $\boldsymbol{u}_1$ is finite at the contact line, the first order stream function will have the form given by

$$\psi_1 = (r/\ell)^2\ln(r/\ell)q_{2L,1}(\theta) + \sum_{n=1}^{\infty}(r/\ell)^n q_{n,1}(\theta). \tag{22}$$

From this stream function, the velocity field and stress tensor can be analytically determined so that first order equivalent of equation (17), taken in the limit as $\epsilon \to \ell_i$, becomes

$$\lim_{\epsilon\to\ell_i}\int_0^{\phi_0} \hat{\boldsymbol{e}}_{\boldsymbol{r}}\cdot(Ca\boldsymbol{T}_{A1})\cdot\hat{\boldsymbol{e}}_{\boldsymbol{x}}rd\theta$$
$$= \lim_{\epsilon\to\ell_i}\int_0^{\phi_0} Ca\left[\ln(r/\ell)h_{2L}(\theta) + \sum_{n=1}^{\infty}(r/\ell)^{n-2}h_n(\theta)\right]rd\theta. \tag{23}$$

Here, h simply denotes the function that collects the terms of $\hat{\boldsymbol{e}}_{\boldsymbol{r}}\cdot(Ca\boldsymbol{T}_{A1})\cdot\hat{\boldsymbol{e}}_{\boldsymbol{x}}$ that scale with the same order of r. In this limit where $\epsilon \to \ell_i$, all terms of the integrand are negligible except the $n = 1$ term. Thus the first order viscous force of fluid A acting at the MCL is given by

$$Caf_{A1,x} = Ca\int_0^{\phi_0} h_1(\theta)d\theta. \tag{24}$$

As $f_{A0,x}$ and $f_{A1,x}$ are of the same order of magnitude and because $Ca \ll 1$, we conclude that the first order force is significantly smaller than the zeroth order force. Similarly, we find that the first order forces due to fluid B and in the y direction are also negligible so that the balance of forces at the MCL is given by equation (18) and (19). In the work by Cox (1986), the first order velocity field and corresponding viscous forces are also neglected as they have a negligible effect on the interface shape when compared to the zeroth order forces.

Based on the finite force results above, we remark that the zeroth order MCL solution is a prime example of the singular mathematical models described by Dussan and Davis (1974), much like the well-known Stokeslet (Guazzelli and Morris, 2011). In both the Stokeslet and the zeroth order MCL solution, the force acting over a small area is modeled as mathematical line with infinite stress and finite force. Therefore, they can be considered physically realistic, at least in regard to conservation of mass and momentum. In the context of moving contact lines, it may appear unusual for a model to contain a singular stress and finite force. However, we emphasize that the Stokeslet, potential line source, and potential line vortex all exhibit the same characteristics and have all been successfully used in modeling a wide variety of physical phenomena. In the following discussion, we present a complex formulation of the MCL problem that yields the same finite force at the MCL, but avoids some of the algebra through the use of Cauchy's residue theorem.

Complex formulation of the moving contact line force

In the analysis above, the steps required to find the MCL force can be some what cumbersome and therefore, we introduce a relatively simpler complex formulation of the problem in this section. The advantages of this formulation will become clear in §6, when the MCL problem is compared with the Stokeslet and cusped fluid interface.

As demonstrated by Langlois and Deville (1964), any flow satisfying the Stokes equation will ensure that the pressure and vorticity are harmonic conjugates. Thus, we can define the function $G = \mu\omega + ip$ representing the shear and normal stresses. For the zeroth order solution, G_0 is given by

$$G_0 = \mu\omega_0 + ip_0 = 2\mu U\frac{-D + iC}{z}. \tag{25}$$

It is immediately apparent that G_0 has a simple pole at the location of the contact line where $z = 0$ and represents a dipole distribution. Furthermore, we observe that the complex function G and the reduced stress tensor $\hat{\boldsymbol{T}}$ are composed of pressure and vorticity only. Thus, it is not all that surprising that the contour integral of $\hat{\boldsymbol{T}}$ can be written in terms of a complex contour integral of G, that is

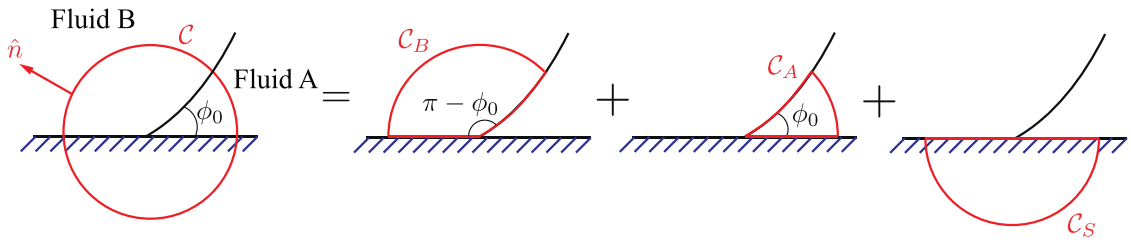

Fig. 5. Decomposition of the contour $\mathcal{C}$ into $\mathcal{C}_A$, $\mathcal{C}_B$, and $\mathcal{C}_S$.

$$\begin{aligned}\oint G dz &= \oint (\mu\omega + ip)(dx + idy)\\ &= \oint (-p\hat{\boldsymbol{e}}_{\boldsymbol{x}} - \mu\omega\hat{\boldsymbol{e}}_{\boldsymbol{y}}) \cdot \left(\frac{dy}{ds}\hat{\boldsymbol{e}}_{\boldsymbol{x}} - \frac{dx}{ds}\hat{\boldsymbol{e}}_{\boldsymbol{y}}\right) ds\\ &\quad + i\oint (\mu\omega\hat{\boldsymbol{e}}_{\boldsymbol{x}} - p\hat{\boldsymbol{e}}_{\boldsymbol{y}}) \cdot \left(\frac{dy}{ds}\hat{\boldsymbol{e}}_{\boldsymbol{x}} - \frac{dx}{ds}\hat{\boldsymbol{e}}_{\boldsymbol{y}}\right) ds\\ &= \oint \hat{\boldsymbol{n}} \cdot \hat{\mathbf{T}} \cdot \hat{\boldsymbol{e}}_{\boldsymbol{x}} ds + i\oint \hat{\boldsymbol{n}} \cdot \hat{\mathbf{T}} \cdot \hat{\boldsymbol{e}}_{\boldsymbol{y}} ds. \end{aligned} \tag{26}$$

Here, the real and imaginary components are exactly equal to the stress integral terms of equations (14) and (15) and correspond to the viscous force exerted by the fluid in the x and y directions. In contrast to the previous analysis, this formulation reveals that we can avoid the tedious algebra of integrating $\hat{\boldsymbol{T}}$, and instead evaluate the left hand side of equation (26) using Cauchy's method of residues (Mitrinovic and Keckic, 1984). However, the standard residue theorem cannot be applied over the contour $\mathcal{C}$, as the function G is piecewise holormophic within the contour. Therefore, it is necessary to decompose the contour $\mathcal{C}$ into the three subcontours $\mathcal{C}_A$, $\mathcal{C}_B$, and $\mathcal{C}_S$ that enclose each phase, see Fig. 5. Inside each subcontour, G is entirely holomorphic and the pole resides at the MCL ($z = 0$). Thus, we can treat the contour integral of G_A and G_B using Cauchy's residue theorem and the Sokhotski-Plemelj formulas (Estrada and Kanwal, 2012). For the zeroth order solution, we obtain

$$\oint_{\mathcal{C}} G_0 dz = \oint_{\mathcal{C}_A} G_{A0} dz + \oint_{\mathcal{C}_B} G_{B0} dz + \oint_{\mathcal{C}_S} G_S dz,$$

$$\oint_{\mathcal{C}_A} G_{A0} dz = \phi_0 i \,\mathrm{Res}(G_{A0}) = -2\phi_0\mu_A U C_A - i2\phi_0\mu_A U D_A,$$

$$\begin{aligned}\oint_{\mathcal{C}_B} G_{B0} dz &= (\pi - \phi_0) i \,\mathrm{Res}(G_{B0})\\ &= -2(\pi - \phi_0)\mu_B U C_B - i2(\pi - \phi_0)\mu_B U D_B.\end{aligned}$$

Additional details regarding the Sokhotski-Plemelj formulas and the treatment of singularities residing on the contour can be found in Appendix C. As before, the integral of G_S is the force exerted by the stress of the solid.

The real component of the complex contour integrals above can be substituted into equation (16), and we once again obtain equation (18), representing the balance of viscous and surface tension forces at the MCL. Similarly the imaginary components can be used to obtain equation (19). Interestingly, one can use the complex contour integral of G to find the total surface force for any Stokes flow. As we will show in §6, this complex analysis correctly captures the viscous force exerted by two other singular Stokes flows that have similar pressure and vorticity fields. While we have only presented a relatively simple complex formulation relevant to the MCL force, complex variables can also be used to define the stream function and velocity to analytically solve for viscous flows in a variety of problems (Crowdy and Brzezicki, 2017; Crowdy and Or, 2010). In the following section, we compare our result to previous works and discuss the physical implications and limitations of this solution.

4. Discussion of the MCL force

The analysis of the previous section shows that the force at the moving contact line predicted by the Stokes solution is finite. However, previous works (Batchelor, 1967; Huh and Scriven, 1971) have reported a logarithmically infinite total force on the solid. So why does the analysis above predict a finite force when others report an infinite force? To understand the distinction, we first replicate the result of Huh & Scriven, by integrating the stress of fluid A along *only* the fluid-solid boundary, i.e.

$$f_{AS,x} = \int_0^R \hat{\boldsymbol{e}}_{\boldsymbol{\theta}} \cdot \boldsymbol{T}_{A0} \cdot \hat{\boldsymbol{e}}_{\boldsymbol{x}} dr \quad \text{at} \quad \theta = 0^\circ, \tag{27}$$

where R is some finite length. From the solution provided in Appendix B, one can show that $\hat{\boldsymbol{e}}_{\boldsymbol{\theta}} \cdot \boldsymbol{T}_{A0} \cdot \hat{\boldsymbol{e}}_{\boldsymbol{x}} = -\mu_A\omega_{A0}$, and that the integral above is improper, as ω_{A0} is singular at $r = 0$. Therefore, this integral can only be evaluated in the limit, that is

$$\begin{aligned}f_{AS,x} &= \lim_{\epsilon\to 0}\int_\epsilon^R -\frac{2\mu_A U}{r}[C_A\sin(0) - D_A\cos(0)]dr\\ &= \lim_{\epsilon\to 0} 2\mu_A D_A U[\ln R - \ln\epsilon]\\ &= \infty.\end{aligned}$$

Thus, the viscous force exerted by fluid A along the fluid-solid interface is logarithmically infinite. The same analysis performed for fluid B at $\theta = 180^\circ$ yields another infinite force. *Individually*, fluid A and B exert infinite forces along the fluid-solid interface, however, the sum of these two infinite forces is undefined or infinite depending on the sign of D. Note that in this approach, only the forces along the fluid-solid interface are considered. This would contradict Young's equation, which clearly includes the surface tension force of the fluid-fluid interface that only exists at $r = 0$ on the solid boundary, and nowhere else.

Based on the discussion above, we find that the distinction between our analysis and previous results, is the control volume that is used to derive the force integral. In the analysis of Huh & Scriven, the force integral given by equation (27) is derived for rectangular control volumes containing discontinuities across a two-dimensional manifold or surface, i.e. a fluid interface (Leal, 2007). In contrast, the force integral presented in equation (17) is specifically derived for volumes containing line discontinuities like the contact line and thus includes the forces acting along the fluid-fluid interface. In works that report an infinite force, it appears that the MCL was viewed as an extension of the interface between a single fluid and solid. Thus, the force was determined by integrating the fluid stress along the fluid-solid interface only. However, the MCL is *not* an extension of a fluid-solid interface, but rather a line defined by the intersection of three immiscible materials. From this perspective, it is natural to define a control volume that encloses all three materials and the MCL. In related analyses of the contact line Slattery et al. (2007) and Andreotti and Snoeijer (2016) have also chosen the same cylindrical control volume. By defining the control volume in this fashion, we include the forces that act on the fluid-fluid interface and capture the multivalued nature of the MCL.

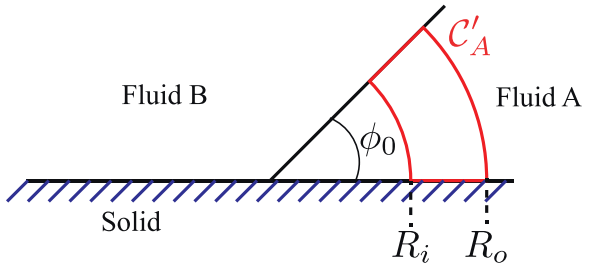

Fig. 6. Annular contour $\mathcal{C}'_A$ (shown in red) with inner radius R_i and outer radius R_o residing in fluid A. (For interpretation of the references to colour in this figure legend, the reader is referred to the web version of this article.)

To physically understand why the total force at the MCL remains finite, consider the annular contour $\mathcal{C}'_A$ with inner radius R_i and outer radius R_o that lies inside fluid A, as shown in Fig. 6. In the zeroth order solution, the stress along the two radial segments and the stress along the two azimuthal segments are exactly equal and opposite, that is

$$\underbrace{-\left[\hat{\boldsymbol{e}}_{\boldsymbol{\theta}} \cdot \hat{\boldsymbol{T}}_{A0} \cdot \hat{\boldsymbol{e}}_{\boldsymbol{x}}\right]_{\theta=0}}_{\text{fluid-solid interface}} = \underbrace{\left[\hat{\boldsymbol{e}}_{\boldsymbol{\theta}} \cdot \hat{\boldsymbol{T}}_{A0} \cdot \hat{\boldsymbol{e}}_{\boldsymbol{x}}\right]_{\theta=\phi_0}}_{\text{fluid-fluid interface}} = -\frac{2\mu_A U D_A}{r},$$

$$\underbrace{-\left[(\hat{\boldsymbol{e}}_{\boldsymbol{r}} \cdot \hat{\boldsymbol{T}}_{A0} \cdot \hat{\boldsymbol{e}}_{\boldsymbol{x}})r\right]_{r=R_i}}_{\text{inner arc}} = \underbrace{\left[(\hat{\boldsymbol{e}}_{\boldsymbol{r}} \cdot \hat{\boldsymbol{T}}_{A0} \cdot \hat{\boldsymbol{e}}_{\boldsymbol{x}})r\right]_{r=R_o}}_{\text{outer arc}} = -2\mu_A U C_A.$$

Thus, the force acting along the fluid-fluid interface is balanced by the force acting along the fluid-solid interface. Similarly, the forces along the two azimuthal arcs balance each other and the total surface force acting on the contour $\mathcal{C}'_A$ is zero, as expected given Eq. 20. If we shrink the radius of the inner arc to zero, the contour $\mathcal{C}'_A$ is reduced to $\mathcal{C}_A$ and passes through the singularity, as shown in Fig. 5. Here, the logarithmically infinite force along the fluid-solid interface is balanced by the force along the fluid-fluid interface, as the stress along each boundary approaches positive and negative infinity at the same rate. A similar cancellation of logarithmic singularities is reported in the work of Jones (2003) when the free vortex sheet is shed tangentially from the plate edge. In the end, the total force exerted by the fluid is given by the azimuthal arc and remains finite no matter how small $\mathcal{C}_A$ becomes.

While the analysis above demonstrates that there is a finite force at the MCL, the model is not without its limitations. One such limitation is the viscous dissipation per unit volume, which scales as r^{-2}. This dissipation is non-integrable for both fluids and results in a singular total energy. However, this does not affect the balance of momentum so long as density and viscosity are constant. This singular energy is not unique to the MCL problem and appears in several other two-dimensional singular continuum models. For example, the potential line source/sink and line vortex have infinite kinetic energy at the singularity (Batchelor, 1967). From electromagnetism, the energy per unit volume for an infinite line charge or infinitely long current carrying wire is also singular (Griffiths, 1972). These singular magnitudes in energy are a consequence of modeling some finite sized physical feature as a mathematical line, where some desired integral quantity is preserved. For example, the potential line vortex is the limiting case of a Rankine vortex where the radius of the central core is reduced to zero while preserving the total circulation. In this limit, circulation can only be preserved if angular velocity approaches infinity, therefore, the potential line vortex exhibits infinite kinetic energy. Despite this non-physical kinetic energy, potential flow theory has successfully modeled a wide range of high Reynolds number flows. Similarly, the MCL model presented in this manuscript is the limit where the fluid slip region has been reduced to an infinitely small point while preserving the total force. We recognize that these singular continuum models are idealized representations of the true physical phenomena. For the MCL problem, this relatively simple model will require additional development in order to capture the transfer of energy. However, it is still valid when considering forces and momentum transfer near the MCL. In the following section, we explore the impact of this model on the prediction of dynamic contact angle.

5. Dynamic contact angle model

The force balance presented above is essentially a dynamic Young's equation that can be used to model the dynamic contact angle. To do so, we assume that the solid is relatively rigid such that any deformation of the solid near the MCL is extremely small (Lester, 1961; Slattery et al., 2007). As a result, $f_{S,x}$ is small relative to the other terms of equation (18) and the force balance at the contact line can be written as

$$2\phi_0\mu_A U C_A + 2(\pi - \phi_0)\mu_B U C_B - \sigma_{AB}\cos(\phi_0) = \sigma_{AS} - \sigma_{BS}. \tag{28}$$

In the equation above, the viscosity, interface velocity, and surface tension are known and therefore one can solve for the only remaining unknown variable, namely the dynamic contact angle ϕ_0. This angle corresponds to the microscopic contact angle since equation (28) represents the force balance at $r = \ell_i$. For the idealized hydrodynamic solution, $\ell_i = 0$ and ϕ_0 is the microscopic angle measured at the solid surface. In problems where slip occurs over a finite but significantly smaller length than the capillary length ($\ell_i \ll \ell_c$), ϕ_0 corresponds to the microscopic angle measured just outside the slip region. In the limit $U \to 0$, equation (28) is simplified to the static Young's equation. The static Young's equation can be used to replace the right hand side of equation (28) with $-\sigma_{AB}\cos(\phi_{\text{static}})$ so that the dimensionless dynamic Young's equation is rewritten as

$$\cos(\phi_0) - \cos(\phi_{\text{static}}) = Ca_A[2\phi_0 C_A + 2(\pi - \phi_0)C_B\lambda]. \tag{29}$$

This non-dimensional form reveals that the change in microscopic contact angle scales with Capillary number and is consistent with diffuse interface and molecular kinetic models. The diffuse interface model predicts that microscopic contact angle will scale as

$$\cos(\phi_0) - \cos(\phi_{\text{static}}) \sim Ca\frac{\zeta}{\ell_s}, \tag{30}$$

where ζ is the fluid-solid interface width (Qian et al., 2003, 2006). Ren and E. (2007) propose a similar model except the change in contact angle is also dependent on the thickness of the fluid-fluid interface and a phenomenological friction coefficient. Molecular kinetic theory proposes the relation

$$\cos(\phi_0) - \cos(\phi_{\text{static}}) = CaF_B(\nu_0, \xi), \tag{31}$$

where F_B is a Boltzman factor that is a function of the molecular equilibrium frequency and molecular displacement, ν_0 and ξ (Blake, 2006; Blake and Coninck, 2011; Snoeijer and Andreotti, 2013). The right hand side of equations (29)–(31) show that the change in microscopic contact angle scales with Capillary number multiplied by a factor representing the proposed physical mechanisms of each model. In our proposed model, the factor on the right hand side represents the total viscous force acting on the contact line region and only contains macroscopic parameters that are known a priori, e.g. viscosity. In contrast, microscopic parameters used in other models such as the interface thickness, molecular displacement, and molecular equilibrium frequency are typically fitted from experimental data (Blake, 2006). Interestingly, we have not specified the physical mechanism which regularizes the stress singularity at microscopic scales, whether it be slip or

Table 1
Fluid properties of Brookfield std. viscosity fluid and 70% glycerol solution investigated by Hoffman (1975) and Blake and Shikhmurzaev (2002), respectively.

	μ [N s/m^2]	ρ [kg/m^3]	σ_{AB} [N/m]	ϕ_{static}
Brookfield std. viscosity fluid	98.8	974	0.0217	0°
70% glycerol solution	0.023	1181	0.0635	67°

molecular attachment and detachment. So long as the inner flow is governed by the Stokes equation, path independence of the stress integral means that regardless of the microscopic physical mechanisms, the total force must equal the net change in fluid momentum. As conservation of momentum must be satisfied for any physical model, it is somewhat expected that equations (29)–(31) are similar in form. Among these models there are subtle differences in how the contact line region is defined. In the work by Qian et al. (2003, 2006), the contact line is defined only as the lower boundary of the fluid-solid interface. Ren and E. (2007) define a microscopic pill box that sits on the solid surface and encloses the fluid-solid and fluid-fluid interface. In this manuscript, we define the contact line region by $r < \ell_i$. These differing definitions of the contact line region also leads to slightly different viewpoints on the length scale at which the microscopic contact angle is defined. Despite these differences, these models can still be reasonably compared because Cox (1986) demonstrated that within the inner region, the interface is approximately planar and the contact angle is not dependent on distance from the contact line (see page 176). As discussed in §3, path independence of the stress integral in Stokes flows allows us to model this inner region as a sharp line if the length scale of the problem of interest is much larger than ℓ_i. The sharp line limit of the MCL is simply the extension of the sharp interface limit from a mathematical surface to a line.

To demonstrate the utility of this model, we apply it to the Brookfield std. viscosity fluid and 70% glycerol solution, whose dynamic contact angles were experimentally measured by Hoffman (1975) and Blake and Shikhmurzaev (2002), respectively. In this example, these two fluids and experiments are chosen for their contrasting fluid properties and experimental set ups. However, the same analysis can be applied to other fluids and geometries as well. As shown in Table 1, the Brookfield fluid has a high viscosity and perfectly wets the solid while the glycerol solution has a significantly lower viscosity and only partially wets the solid. With respect to the experimental set up, Hoffman measured the contact angle of a liquid slug as it was pushed through a 1.95 mm precision bore tube while Blake & Shikhmurzaev measured the dynamic contact angle created by plunging a smooth tape into a bath of fluid. Despite these two very different fluids and experiments, we will see that the theoretical model is in good agreement with the experimental measurements.

Given the fluid properties in Table 1, we use equation (28) to obtain a theoretical prediction of microscopic dynamic contact angle as a function of Capillary number, as shown in Fig. 7(a). To account for the roughness of the solid surface we have used $\phi(Ca \to 0^+)$ in place of ϕ_{static} in equation (28). At first glance, we observe that the glycerol solution exhibits a relatively smaller change in contact angle as Ca increases. This is due to the significantly larger viscosity ratio that allows the Brookfield fluid to more easily reduce the contact angle of the receding air phase. To compare our results with those reported by Hoffman and Blake & Shikhmurzaev, we combine our model for microscopic contact angle (ϕ_0) with Cox's model for apparent contact angle (ϕ_D) (Cox, 1986). Cox's zeroth order model is given by

$$g(\lambda, \phi_D) = g(\lambda, \phi_0) + Ca \ln(1/\varepsilon), \tag{32}$$

where all terms are of order 1 and $\varepsilon = \ell_i/\ell_o$ is the ratio of the inner length scale to the outer length scale. $g(\lambda, \phi)$ is given by

$$g(\lambda,\phi) = \int_0^{\phi} \frac{\lambda(\beta^2 - \sin^2\beta)[(\pi-\beta) + \sin\beta\cos\beta] + [(\pi-\beta)^2 - \sin^2\beta](\beta - \sin\beta\cos\beta)}{2\sin\beta[\lambda^2(\beta^2\sin^2\beta) + 2\lambda\{\beta(\pi-\beta) + \sin^2\beta\} + \{(\pi-\beta)^2 - \sin^2\beta\}]} d\beta.$$

In contrast to the dynamic Young's equation which captures the total force acting over the inner region $r \le \ell_i$, Cox's model captures the viscous bending of the fluid interface between ℓ_i and ℓ_c along the fluid-fluid interface (Blake, 2006). The apparent contact angle predicted by the combination of these two models is shown in Fig. 7(b) with $\varepsilon = 10^{-4}$. Note that the outer length scale is the distance at which the apparent contact angle is measured and is often interpreted as the capillary length scale. Hoffman and Blake & Shikhmurzaev did not report the length scale of their contact angle measurements, however it was likely smaller than the capillary length scale due to their use of microscopes. Consequently, experimentally obtained values of ε are slightly larger than one might expect if one were to use the capillary length as the outer length scale.

Overall, there is good agreement between the theoretical apparent dynamic contact angle and the experimental data of both Hoffman and Blake & Shikhmurzaev. At low Ca, the current model diverges slightly from the experimental data of the glycerol solution. This difference could be created by errors in contact angle measurement or by differences in the way apparent contact angle is defined. In Fig. 8 we provide additional comparisons for the remaining fluids that were tested by Hoffman and Blake & Shikhmurzaev. In this figure the magnitude of $g(\lambda, \phi_D) - g(\lambda, \phi_0)$ is plotted against $Ca\ln(1/\varepsilon)$ so that the model can be represented by a single curve regardless of static contact angle or viscosity ratio. As before, the microscopic contact angle is predicted by equation (28) and the combined model captures the dynamic contact angle behavior. There is some deviation at high Ca, however this is to be expected as the current model is derived by assuming $Ca \ll 1$. In a recent experimental work, we have found additional support for this finite MCL force model by accurately capturing the microscopic dynamic contact angle using a dynamic Wilhelmy plate (Zhang and Mohseni, 2019). The results presented here can be extended to receding contact lines by combining our model with the model proposed by Eggers (2004, 2005). One only needs to substitute negative values of U into equation (28) so that the advancing and receding fluids are reversed.

In this current model, ϕ_0 is a function of Ca and is in agreement with the experimental observations of Ramé et al. (2004). However, the finite force analysis does not provide a theoretical means of determining the length scale ratio, ε. Regardless, we found that the results are not particularly sensitive to ε (in agreement with Bonn et al., 2009) and therefore a constant value of 10^{-4} was used for all experimental comparisons despite the different fluid properties. This suggests that, at least for these test cases, ε could be treated as a constant that is independent of the fluid properties and experimental set up.

In addition to providing a theoretical model of the dynamic contact angle, the results above will impact other aspects of

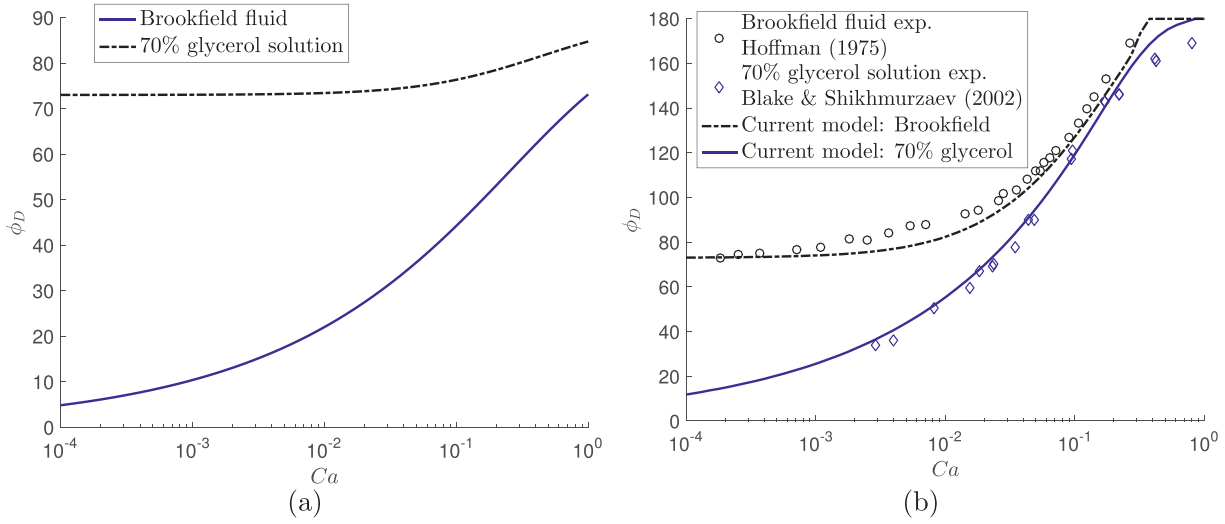

Fig. 7. (a) Microscopic dynamic contact angle predicted for the Brookfield fluid and 70% glycerol solution investigated by Hoffman (1975) and Blake and Shikhmurzaev (2002), respectively. Microscopic dynamic contact angle is obtained using equation (28) and the MCL solution presented in §2. (b) Apparent dynamic contact angle comparison between experimental measurements and current theoretical model. The current work uses the model from Cox (1986) where the microscopic contact angle, ϕ_0, is theoretically predicted by equation (28).

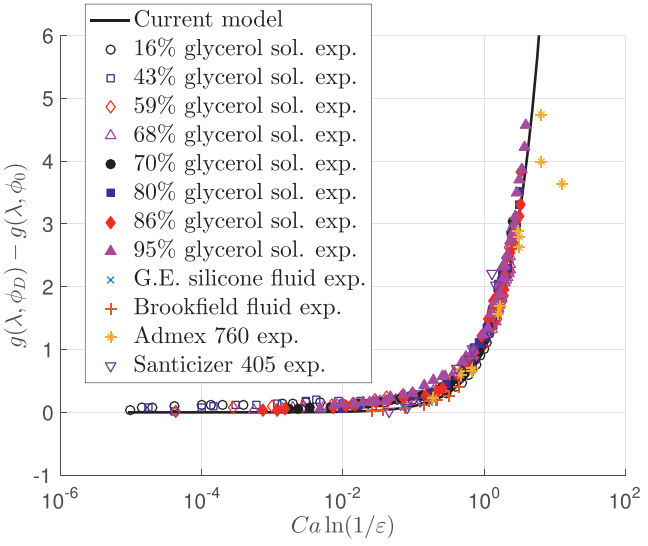

Fig. 8. Comparison of the current model to experimental data measured by Hoffman (1975) and Blake and Shikhmurzaev (2002). All glycerol solution data points were adapted from Blake and Shikhmurzaev (2002) while the remaining data points were adapted from Hoffman (1975). To collapse the model regardless of static contact angle or viscosity ratio, the data is presented as $g(\lambda,\phi_D) - g(\lambda,\phi_0)$ vs. $Ca\ln(1/\varepsilon)$ where $\varepsilon = 10^{-4}$.

MCL dynamics. For example, microscopic contact angle determines the sign and strength of vorticity near the MCL (Zhang and Mohseni, 2018) as well as the surface tension force which is given by $\sigma\cos\phi_0$. These effects are important in microfluidics and heat/mass transfer applications where vorticity and surface tension forces influence mixing and contact line pinning. Furthermore, this result may be useful in numerical simulations where physical phenomena of interest typically span several orders of magnitude. Convergence of numerical solutions are extremely sensitive to the prescribed contact angle and grid size (Afkhami, Zaleski, Bussmann, 2009). In general, grid convergence is achieved when the grid resolution of the simulation is the same order of magnitude as the slip length, typically 10^{-7}m to 10^{-9}m for water. Thus, the required number of grid points for most simulations is extremely large. In order to reduce the computational cost and improve accuracy, the Stokes flow solution could be used as a subgrid model. In such a scheme, the minimum grid size would be determined by the validity of the small *Re* assumption. The implementation of a Stokes flow subgrid model is outside the scope of this publication, but will be investigated in future works.

6. Comparison with similar singular stokes flows

While unfamiliar in the context of a moving contact line, a finite force corresponding to a singular stress is not unprecedented. In fact, there exist two other Stokes flows that contain stress singularities and that have known finite forces, namely the cusped interface flow and Stokeslet. The cusped interface flow, investigated by Richardson (1968) and Joseph et al. (1990), is created by two submerged cylinders rotating with constant angular velocity. Under the right conditions, the fluid interface will develop a cusp singularity. The stream function near a cusped interface is reported by Richardson as

$$\psi = \frac{\sigma}{2\pi\mu} r\ln(r)\sin(\theta).$$

It is easily shown that the complex formulation of this flow is given by

$$G = \mu\omega + ip = -\frac{\sigma i}{\pi z}.$$

Evaluating equation (26) using Cauchy's residue theorem for a singularity that lies on the contour and at a cusp yields a force per unit length of $f = 2\sigma$, in agreement with Richardson.

A similar analysis can be performed for a two-dimensional Stokeslet, i.e. the flow that is created by an infinitely small cylinder moving through a quiescent fluid (Avudainayagam and Jothiram, 1987; Guazzelli and Morris, 2011). For a Stokeslet that is aligned with the x-axis, the stream function and complex function G are given by

$$\psi = \frac{\alpha}{4\pi} r\sin(\theta)[1 - \ln(r)],$$

$$G = \mu\omega + ip = \frac{\mu\alpha i}{2\pi z},$$

where α is the strength of the Stokeslet. Evaluating equation (26) for a contour path that encloses the Stokeslet

yields a force per unit length of $f = -\mu\alpha$. This result is consistent with the force reported by Avudainayagam and Jothiram (1987). As discussed previously, the viscous surface force in a Stokes flow is solely determined by the pressure and vorticity. From the complex function G, we see that despite the different velocity fields, both the Stokeslet and the cusped fluid interface have vorticity and pressure fields that take the form of a dipole. In addition to a singular stress and finite force, we also note that the Stokeslet, cusped interface, and MCL singularity all predict infinite viscous dissipation per unit volume at $r = 0$. While this dissipation is singular, numerous applications of the Stokeslet singularity (Crowdy and Or, 2010; Pozrikidis, 1990) have demonstrated that the finite force predicted by these singular models can still be used to model physical problems.

7. Concluding remarks

In this publication, the force at a moving contact line was theoretically investigated using the hydrodynamic solution of the MCL. By defining a cylindrical control volume around the MCL, we were able to show using both real and complex analysis that the total viscous force exerted by the fluids on the solid is finite despite a singular stress. Unlike previous treatments of the contact line, this control volume accounts for the viscous forces that act on the fluid-fluid interface in addition to the forces that act on the fluid-solid interface, much like the Young's equation. With this finite force, we proposed a model for microscopic dynamic contact angle that is a function of the interface velocity, fluid viscosity, and surface tension. As validation, we combined our model for microscopic contact angle with Cox's model for apparent contact angle and achieved a good match with experimental measurements. Interestingly, the results reported in this work have been alluded to in previous publications. Cox recognized the possibility of a velocity dependent microscopic contact angle and stated "it is uncertain whether such an angle [microscopic angle] would depend on the spreading velocity" (Cox, 1986). In a more direct observation, Voinov (1976) stated "In this case α_m [microscopic angle] can be a function of the velocity". Dussan and Davis (1974) recognized the similarities between the MCL problem and other singular models which led them state: "There exist physical situations where the force distributed over a small area is replaced by a force acting at a point or a line. (This implies an unbounded stress tensor)". In the end, we would like to emphasize that the analysis and conclusions made in this work are for a MCL *model* much like the Stokeslet and cusped fluid interface. The finite force result does not imply that phenomena like slip or thermal activation do not occur, but merely that the net effect of these microscopic phenomena should yield the same total change in momentum within a microscopic control volume enclosing the contact line.

In the field of wetting and dewetting, the concept of a finite force despite a singular stress is somewhat unusual. However, if we look to other fields, we find that there are many two-dimensional singular continuum models with similar characteristics. In electromagnetism, electric fields are singular at the locations of line charges. Through Gauss' law, we know that the strength of the point charge is finite despite the fact that the electric field is singular. In potential flow theory, line sources and line vortices are regularly used to model flows at high Reynolds numbers. Despite the fact that the velocity or shear stress approaches infinity at these singularities, they still conserve physical quantities such as mass flux and circulation. These singular models do not resolve the exact physics that occur at the singularity and are capable of correctly capturing the global features of the problem. In this sense, there may be fluid slip extremely close to the moving contact line, however we do not need to resolve it as we can already obtain the contact line force and nearby velocity field. Essentially the finite force at the moving contact line is merely a different physical application of the same mathematical concepts that are applied in other fields. At present, the MCL model retains a singular stress and infinite viscous dissipation at the corner singularity and are known limitations of this model. Motivated by the results of this work, future works will seek to extend this model to accurately capture the transfer of energy at the MCL.

Declaration of Competing Interest

The authors declare that they do not have any financial or non-financial conflict of interests

CRediT authorship contribution statement

Peter Zhang: Conceptualization, Methodology, Validation, Formal analysis, Investigation, Data curation, Writing - original draft, Visualization. **Kamran Mohseni:** Conceptualization, Resources, Writing - review & editing, Supervision, Project administration, Funding acquisition.

Acknowledgments

We would like to thank the Office of Naval Research for their support in this research effort. We would also like to thank Dr. Adam DeVoria and Joseph Thalakkottor for their helpful discussion.

Appendix A. General solution to the biharmonic equation

The biharmonic stream function equation is given by

$$\nabla^4\psi = 0. \tag{A.1}$$

In polar coordinates, the solution is found using the technique of separation of variables with $\psi = R(r)\Theta(\theta)$. The solution that was initially reported by Michell (1899), and later extended by Filonenko-Borodich (1958), is given by

$$\psi = (r/\ell)^2 \ln(r/\ell) q_{2L}(\theta) + (r/\ell)\ln(r/\ell) q_{1L}(\theta) + \ln(r/\ell) q_{0L}(\theta) + \sum_{n=-\infty}^{\infty} (r/\ell)^n q_n(\theta). \tag{A.2}$$

The functions q are given by

$$\begin{aligned}
q_{2L} &= P_{2L}[A_{2L} + B_{2L}\theta],\\
q_{1L} &= P_{1L}[A_{1L}\cos(\theta) + B_{1L}\sin(\theta) + C_{1L}\theta\cos(\theta) + D_{1L}\theta\sin(\theta)],\\
q_{0L} &= P_{0L}[A_{0L} + B_{0L}\theta],\\
q_0 &= P_0[A_0 + B_0\theta + C_0\cos(2\theta) + D_0\sin(2\theta)],\\
q_1 &= P_1[A_1\cos(\theta) + B_1\sin(\theta) + C_1\theta\cos(\theta) + D_1\theta\sin(\theta)],\\
q_2 &= P_2[A_2 + B_2\theta + C_2\cos(2\theta) + D_2\sin(2\theta)],\\
q_n &= P_n[A_n\cos((n-2)\theta) + B_n\cos(n\theta) + C_n\sin((n-2)\theta) + D_n\sin(n\theta)] \quad \text{for} \quad n \geq 3,\\
q_n &= P_n[A_n\cos((n+2)\theta) + B_n\cos(n\theta) + C_n\sin((n+2)\theta) + D_n\sin(n\theta)] \quad \text{for} \quad n \leq -1,
\end{aligned}$$

where P is a dimensional coefficient and A, B, C, and D are coefficients determined by the boundary conditions. The velocity, vorticity, and pressure can all be determined using the equations given by

$$\boldsymbol{u} = \boldsymbol{\nabla} \times \psi\hat{\boldsymbol{e}}_{\boldsymbol{z}}, \tag{A.3}$$

$$\omega = -\boldsymbol{\nabla}^2\psi, \tag{A.4}$$

$$\boldsymbol{\nabla} p = \mu\nabla^2\boldsymbol{u}. \tag{A.5}$$

In the past, stream functions of various order r have been investigated individually and correlated to unique classes of flows. The paint scraper problem investigated by Taylor (1962) is described by terms of order $(r/\ell)^{-1}$. Similarly, the MCL problem investigated by Huh and Scriven (1971) is described by terms of order $(r/\ell)^{-1}$. Moffatt eddies and the hinged plate flow correspond to terms with $n \geq 1$ (Moffatt, 1964). The cusped fluid interface and Stokeslet solution investigated by Richardson (1968) and Joseph et al. (1990) is described by terms of order $(r/\ell)\ln(r/\ell)$. Solutions that combine multiple orders of n have been shown to represent more complex flows such as evaporation near the contact line (Gelderblom et al., 2012, 2013).

Appendix B. Zeroth order solution to the moving contact line flow

The zeroth order solution to the moving contact line problem described in §2 was first reported by Moffatt (1964) and Huh and Scriven (1971). In a planar wedge geometry, where fluid A has a contact angle of ϕ_0, the flow is governed by the biharmonic stream function equations given by

$$\nabla^4 \psi_{A0} = 0,$$
$$\nabla^4 \psi_{B0} = 0.$$

The boundary conditions of the zeroth order solution include no-slip at the fluid-solid interface, zero mass flux through all interfaces, and continuity of tangential velocity and shear stress across the fluid-fluid interface. The resulting boundary conditions on ψ_{A0} and ψ_{B0} are therefore given by

$$\psi_{A0}(\theta = 0) = 0, \qquad \psi_{A0}(\theta = \phi_0) = 0,$$
$$\psi_{B0}(\theta = \phi_0) = 0, \qquad \psi_{B0}(\theta = \pi) = 0,$$
$$\left[\tfrac{1}{r}\tfrac{\partial \psi_{A0}}{\partial \theta}\right]_{\theta=0} = U, \qquad \left[\tfrac{1}{r}\tfrac{\partial \psi_{B0}}{\partial \theta}\right]_{\theta=\pi} = -U,$$
$$\left[\tfrac{\partial \psi_{A0}}{\partial \theta}\right]_{\theta=\phi_0} = \left[\tfrac{\partial \psi_{B0}}{\partial \theta}\right]_{\theta=\phi_0}, \qquad \left[\tfrac{\partial^2 \psi_{A0}}{\partial \theta^2}\right]_{\theta=\phi_0} = \left[\lambda \tfrac{\partial^2 \psi_{B0}}{\partial \theta^2}\right]_{\theta=\phi_0},$$

where $\lambda = \mu_B/\mu_A$ denotes the viscosity ratio. Solving the system of equations created by the boundary conditions above yields the stream function, velocity, pressure, and vorticity is given by

$$\psi_0 = rU[A\cos(\theta) + B\sin(\theta) + C\theta\cos(\theta) + D\theta\sin(\theta)],$$
$$u_{0r} = \frac{1}{r}\frac{\partial \psi}{\partial \theta} = U[-A\sin(\theta) + B\cos(\theta) + C[\cos(\theta) - \theta\sin(\theta)] + D[\sin(\theta) + \theta\cos(\theta)]\Big],$$
$$u_{0\theta} = -\frac{\partial \psi}{\partial r} = -U[A\cos(\theta) + B\sin(\theta) + C\theta\cos(\theta) + D\theta\sin(\theta)],$$
$$p_0 = \frac{2\mu U}{r}[C\cos(\theta) + D\sin(\theta)],$$
$$\omega_0 = \frac{2U}{r}[C\sin(\theta) - D\cos(\theta)].$$

For each fluid A, B, C, and D are constant coefficients given by

$$A_A = 0,$$
$$B_A = \frac{(8\phi_0(\lambda-1))\sin(\phi_0)^2 + 4\pi\lambda\phi_0\sin(2\phi_0) + 8\phi_0(\pi^2 - \lambda\phi_0^2 - 2\pi\phi_0 + \phi_0^2 + \pi\lambda\phi_0)}{\Delta},$$
$$C_A = [-8\pi\lambda\sin(\phi_0)^2 + (8\pi\phi_0 - 2\lambda + 4\lambda\phi_0^2 - 4\pi^2 - 4\phi_0^2 - 4\pi\lambda\phi_0 + 2)\sin(2\phi_0) + \lambda\sin(4\phi_0) - \sin(4\phi_0)]/\Delta,$$
$$D_A = \frac{(8-8\lambda)\sin(\phi_0)^4 + (16\pi\phi_0 + 8\lambda\phi_0^2 - 8\pi^2 - 8\phi_0^2 - 8\pi\lambda\phi_0)\sin(\phi_0)^2}{\Delta},$$

$$A_B = \frac{8\pi^2\sin(\phi_0)^2 + (-\pi(4\pi\phi_0 - 2\lambda + 4\lambda\phi_0^2 - 4\phi_0^2 + 2))\sin(2\phi_0) + \pi(\sin(4\phi_0) - \lambda\sin(4\phi_0))}{\Delta},$$
$$B_B = [(8\lambda\phi_0 - 8\phi_0 - 8\phi_0\pi^2 + 8\pi\phi_0^2 - 8\pi\lambda\phi_0^2)\sin(\phi_0)^2 + (2\pi - 2\pi\lambda)\sin(2\phi_0)^2 + (4\pi\phi_0 - 4\pi^2)\sin(2\phi_0) + 8\phi_0\pi^2 - 16\pi\phi_0^2 - 8\lambda\phi_0^3 + 8\phi_0^3 + 8\pi\lambda\phi_0^2]/\Delta,$$
$$C_B = \frac{-8\pi\sin(\phi_0)^2 + (4\pi\phi_0 - 2\lambda + 4\lambda\phi_0^2 - 4\phi_0^2 + 2)\sin(2\phi_0) + \lambda\sin(4\phi_0) - \sin(4\phi_0)}{\Delta},$$
$$D_B = \frac{(8-8\lambda)\sin(\phi_0)^4 + (8\pi\phi_0 + 8\lambda\phi_0^2 - 8\phi_0^2)\sin(\phi_0)^2}{\Delta},$$
$$\Delta = (\phi_0(8\lambda - 8) - 8\pi\lambda)\sin(\phi_0)^2 + ((4\lambda - 4)\phi_0^2 + 8\pi\phi_0 - 2\lambda - 4\pi^2 + 2)\sin(2\phi_0) + (\lambda - 1)\sin(4\phi_0) + (8 - 8\lambda)\phi_0^3 + (8\lambda\pi - 16\pi)\phi_0^2 + 8\pi^2\phi_0.$$

Note that the coefficients are a function of the contact angle, ϕ_0, and viscosity ratio, λ, only.

Appendix C. Complex contour integrals with singularities on the contour

The contour integrals considered in this paper typically contain singularities that are simultaneously on the contour and at a corner. In this section, we demonstrate how Cauchy's residue theorem is affected by singularities on the boundary based on §1.5 of Estrada and Kanwal (2012).

Consider the analytic function $W = 1/(z - \xi)$ and the closed contour C that defines an interior region, S_I, and an exterior region, S_O. The solution to the complex contour integral of W along the path C is given by

$$\oint_C W dz = \begin{cases} 2\pi i, & \xi \in S_I, \\ 0, & \xi \in S_O, \\ \pi i, & \xi \in C \text{ along a smooth segment of C}, \\ \phi i, & \xi \in C \text{ and at a corner}, \end{cases}$$

where the four cases correspond to the location of ξ, as shown in Fig. C.9. In the first two cases, the singularity lies inside the contour ($\xi \in S_I$) or outside the contour ($\xi \in S_O$) and Cauchy's residue theorem yields a solution of $2\pi i\,\mathrm{Res}(W)$ and 0, respectively. If ξ lies on a smooth segment of C, then the Sokhotski-Plemelj theorem states that the integral will equal $\pi i\,\mathrm{Res}(W)$, which in this case is

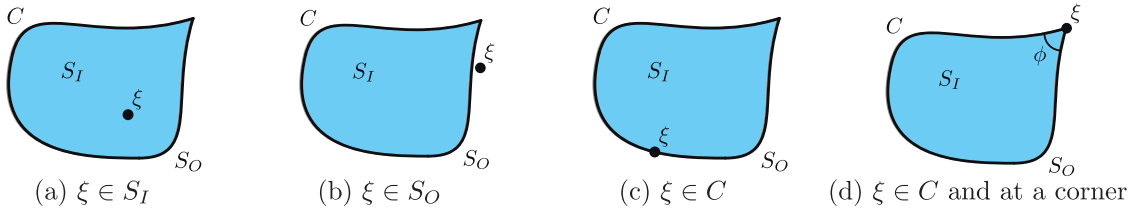

Fig. C9. (a) ξ lies inside the contour in the region S_I (b) ξ lies outside the contour in the region S_O (c) ξ lies on the path C along a smooth segment (d) ξ lies on the path C at a corner point.

πi. If ξ lies on C and at a corner, then the Sokhotski-Plemelj theorem states that the integral will equal $\phi i \,\mathrm{Res}(W) = \phi i$, where ϕ is the angle of the corner.

References

Afkhami, S., Zaleski, S., Bussmann, M., 2009. A mesh-dependent model for applying dynamic contact angles to VOF simulations. J. Comput. Phys. 228 (15), 5370–5389.

Andreotti, B., Snoeijer, J., 2016. Soft wetting and the shuttleworth effect, at the crossroads between thermodynamics and mechanics. Europhys. Lett. 113 (6), 66001.

Avudainayagam, A., Jothiram, B., 1987. No-slip images of certain line singularities in a circular cylinder. Int. J. Eng. Sci. 25 (9), 1193–1205.

Batchelor, G.K., 1967. An introduction to fluid dynamics. Cambridge University Press, Cambridge, UK.

Blake, T., Shikhmurzaev, Y.D., 2002. Dynamic wetting by liquids of different viscosity. J. Colloid Interface Sci. 253 (1), 196–202.

Blake, T.D., 2006. The physics of moving wetting lines. J. Colloid Interface Sci. 299 (1), 1–13. doi:10.1016/j.jcis.2006.03.051.

Blake, T.D., Coninck, J.D., 2011. Dynamics of wetting and kramers' theory. The European Physical Journal Special Topics 197 (1), 249.

Blake, T.D., Haynes, J.M., 1969. Kinetics of liquid/liquid displacement. J. Colloid Interface Sci. 30 (3), 421–423. doi:10.1016/0021-9797(69)90411-1.

Bonn, D., Eggers, J., Indekeu, J., Meunier, J., Rolley, E., 2009. Wetting and spreading. Rev. Mod. Phys. 81, 739–805. doi:10.1103/RevModPhys.81.739.

Cox, R.G., 1986. The dynamics of the spreading of liquids on a solid surface. part 1. viscous flow. J. Fluid Mech. 168, 169–194. doi:10.1017/S0022112086000332.

Crowdy, D., Or, Y., 2010. Two-dimensional point singularity model of a low-reynolds-number swimmer near a wall. Physical Review E 81 (3), 036313.

Crowdy, D.G., Brzezicki, S.J., 2017. Analytical solutions for two-dimensional stokes flow singularities in a no-slip wedge of arbitrary angle. Proc. R. Soc. A 473 (2202), 20170134.

Derby, B., 2010. Inkjet printing of functional and structural materials: fluid property requirements, feature stability, and resolution. Annu. Rev. Mater. Res. 40, 395–414.

Dhir, V.K., 1998. Boiling heat transfer. Annu. Rev. Fluid Mech. 30 (1), 365–401. doi:10.1146/annurev.fluid.30.1.365.

Dussan, E.B., 1976. The moving contact line: the slip boundary condition. J. Fluid Mech. 77 (4), 665–684. doi:10.1017/s0022112076002838.

Dussan, E.B., 1979. On the spreading of liquids on solid surfaces: static and dynamic contact lines. Annu. Rev. Fluid Mech. 11, 371–400. doi:10.1146/annurev.fl.11.010179.002103.

Dussan, E.B., Davis, S.H., 1974. On the motion of a fluid-fluid interface along a solid surface. J. Fluid Mech. 65 (1), 71–95. doi:10.1017/S0022112074001261.

Duvivier, D., Seveno, D., Rioboo, R., Blake, T., Coninck, J.D., 2011. Experimental evidence of the role of viscosity in the molecular kinetic theory of dynamic wetting. Langmuir 27 (21), 13015–13021.

Eggers, J., 2004. Hydrodynamic theory of forced dewetting. Phys. Rev. Lett. 93 (9), 094502.

Eggers, J., 2005. Existence of receding and advancing contact lines. Physics of Fluids 17 (8), 082106.

Eggers, J., Stone, H.A., 2004. Characteristic lengths at moving contact lines for a perfectly wetting fluid: the influence of speed on the dynamic contact angle. J. Fluid Mech. 505, 309–321. doi:10.1017/S0022112004008663.

Eral, H., Oh, J., et al., 2013. Contact angle hysteresis: a review of fundamentals and applications. Colloid Polym. Sci. 291 (2), 247–260.

Estrada, R., Kanwal, R., 2012. Singular integral equations. Springer Science & Business Media.

Filonenko-Borodich, M., 1958. Theory of elasticity. University Press of the Pacific, Moscow.

Gelderblom, H., Bloemen, O., Snoeijer, J., 2012. Stokes flow near the contact line of an evaporating drop. J. Fluid Mech. 709, 69–84.

Gelderblom, H., Stone, H., Snoeijer, J., 2013. Stokes flow in a drop evaporating from a liquid subphase. Physics of Fluids (1994-present) 25 (10), 102102.

de Gennes, P.G., 1985. Wetting: statistics and dynamics. Rev. Mod. Phys. 57, 827–863. doi:10.1103/RevModPhys.57.827.

Griffiths, D.J., 1972. Introduction to electrodynamics. Prentice Hall, Englewood Cliffs, NJ, USA.

Guazzelli, E., Morris, J.F., 2011. A physical introduction to suspension dynamics. Cambridge University Press.

Hocking, L.M., 1977. A moving fluid interface. part 2. the removal of the force singularity by a slip flow. J. Fluid Mech. 79, 209–229.

Hocking, L.M., Rivers, A.D., 1982. The spreading of a drop by capillary action. J. Fluid Mech. 121, 425–442. doi:10.1017/S0022112082001979.

Hoffman, R.L., 1975. A study of the advancing interface. i. interface shape in liquid–gas systems. J. Colloid Interface Sci. 50 (2), 228–241.

Huh, C., Scriven, L.E., 1971. Hydrodynamic model of steady movement of a solid/liquid/fluid contact line. J. Colloid Interface Sci. 35 (1), 85–101. doi:10.1016/0021-9797(71)90188-3.

Jones, M.A., 2003. The separated flow of an inviscid fluid around a moving flat plate. J. Fluid Mech. 496, 405–441. doi:10.1017/S0022112003006645.

Joseph, D.D., Nelson, J., Renardy, M., Renardy, Y., 1990. Two-dimensional cusped interfaces. J. Fluid Mech. 223, 383–409.

Katoh, K., Wakimoto, T., Yamamoto, Y., Ito, T., 2015. Dynamic wetting behavior of a triple-phase contact line in several experimental systems. Exp. Therm Fluid Sci. 60, 354–360.

Landau, L., Levich, B., 1988. Dragging of a Liquid by a Moving Plate. In: Dynamics of Curved Fronts. Elsevier, pp. 141–153.

Langlois, W., Deville, M., 1964. Slow viscous flow. Springer.

Leal, L.G., 2007. Advanced transport phenomena: Fluid mechanics and convective transport processes. Cambridge University Press, New York, NY, USA.

Lester, G., 1961. Contact angles of liquids at deformable solid surfaces. J. Colloid Sci. 16 (4), 315–326.

Michell, J., 1899. On the direct determination of stress in an elastic solid, with application to the theory of plates. Proc. London Math. Soc. 1 (1), 100–124.

Mitrinovic, D., Keckic, J., 1984. The cauchy method of residues: Theory and applications, vol. 259. Springer Science & Business Media.

Moffatt, H.K., 1964. Viscous and resistive eddies near a sharp corner. J. Fluid Mech. 18 (01), 1–18.

Mugele, F., Baret, J.C., 2005. Electrowetting: from basics to applications. J. Phys.: Condens. Matter 17 (28), 705–774. doi:10.1088/0953-8984/17/28/R01.

Navier, C.L.M.H., 1823. Memoire Sur Les Lois Du Mouvement Des Fluides. In: Memoires de l Academie Royale des Sciences de l Instituede France, Vol. 6, Royale des Sciences l Instituede France, pp. 389–440.

Petrov, P., Petrov, I., 1992. A combined molecular-hydrodynamic approach to wetting kinetics. Langmuir 8 (7), 1762–1767.

Pismen, L., 2002. Mesoscopic hydrodynamics of contact line motion. Colloids Surf., A 206 (1–3), 11–30.

Pozrikidis, C., 1990. The axisymmetric deformation of a red blood cell in uniaxial straining stokes flow. J. Fluid Mech. 216, 231–254.

Qian, T., Wang, X.-P., Sheng, P., 2003. Molecular scale contact line hydrodynamics of immiscible flows. Physical Review E 68 (15), 1–15. doi:10.1103/PhysRevE.68.016306. 016306

Qian, T., Wang, X.-P., Sheng, P., 2006. A variational approach to moving contact line hydrodynamics. J. Fluid Mech. 564, 333–360.

Quéré, D., 2008. Wetting and roughness. Annu. Rev. Mater. Res. 38, 71–99.

Ramé, E., Garoff, S., 1996. Microscopic and macroscopic dynamic interface shapes and the interpretation of dynamic contact angles. J. Colloid Interface Sci. 177 (1), 234–244.

Ramé, E., Garoff, S., Willson, K., 2004. Characterizing the microscopic physics near moving contact lines using dynamic contact angle data. Physical Review E 70, 031608. doi:10.1103/PhysRevE.70.031608.

Ren, W., E., W., 2007. Boundary conditions for the moving contact line problem. Physics of Fluids 19 (2), 1–15. doi:10.1063/1.2646754. 022101

Richardson, S., 1968. Two-dimensional bubbles in slow viscous flows. J. Fluid Mech. 33 (03), 475–493.

Seppecher, P., 1996. Moving contact lines in the cahn-Hilliard theory. J. Comput. Phys. 34 (9), 977–992. doi:10.1016/0020-7225(95)00141-7.

Seveno, D., Vaillant, A., Rioboo, R., Adao, H., Conti, J., Coninck, J.D., 2009. Dynamics of wetting revisited. Langmuir 25 (22), 13034–13044.

Shen, C., Ruth, D.W., 1998. Experimental and numerical investigations of the interface profile close to a moving contact line. Physics of Fluids 10 (4), 789–799.

Sheng, P., Zhou, M., 1992. Immiscible-fluid displacement: contact-line dynamics and the velocity-dependent capillary pressure. Physical review A 45 (8), 5694.

Shikhmurzaev, Y.D., 1997. Moving contact lines in liquid/liquid/solid systems. J. Fluid Mech. 334, 211249.

Shikhmurzaev, Y.D., 2006. Singularities at the moving contact line. mathematical, physical and computational aspects. Physica. D 217 (2), 121–133. doi:10.1016/j.physd.2006.03.003.

Shikhmurzaev, Y.D., 2007. Capillary flows with forming interfaces. CRC Press.
Sibley, D.N., Nold, A., Kalliadasis, S., 2015. The asymptotics of the moving contact line: cracking an old nut. J. Fluid Mech. 764, 445–462.
Slattery, J.C., Sagis, L., Oh, E.S., 2007. Interfacial transport phenomena, 2nd Springer, New York, New York, NY, USA.
Snoeijer, J.H., 2006. Free-surface flows with large slopes: beyond lubrication theory. Physics of Fluids 18 (2), 021701.
Snoeijer, J.H., Andreotti, B., 2013. Moving contact lines: scales, regimes, and dynamical transitions. Annu. Rev. Fluid Mech. 45, 269–292. doi:10.1146/annurev-fluid-011212-140734.
Sui, Y., Ding, H., Spelt, P.D.M., 2014. Numerical simulations of flows with moving contact lines. Annu. Rev. Fluid Mech. 46, 97–119. doi:10.1146/annurev-fluid-010313-141338.
Sui, Y., Spelt, P.D., 2013. Validation and modification of asymptotic analysis of slow and rapid droplet spreading by numerical simulation. J. Fluid Mech. 715, 283–313.
Taylor, G., 1962. On Scraping Viscous Fluid from a Plane Surface. In: Miszellangen der Angewandten Mechanik (Festschrift Walter Tollmien), pp. 313–315.
Thalakkottor, J.J., Mohseni, K., 2016. Universal slip boundary condition for fluid flows. Physical Review E 94, 023113. doi:10.1103/PhysRevE.94.023113.
Zhang, Peter, Mohseni, Kamran, 2018. Dipole model of vorticity at the moving contact line. Int. J. of Multiphase Flow 103, 169–172.
Zhang, Peter, Mohseni, Kamran, 2019. Viscous drag force model for dynamic Wilhelmy plate experiments. Physical Review Fluids 4, 084004. doi:10.1103/PhysRevFluids.4.084004.
Thalakkottor, J.J., Mohseni, K., 2019. The role of surface tension gradient in determining microscopic dynamic contact angle. ArXiv preprint arXiv:1803.05931v1.
Thompson, P.A., Troian, S.M., 1997. A general boundary condition for liquid flow at solid surfaces. Nature 389 (6649), 360–362. doi:10.1038/38686.
Vandre, E., Carvalho, M., Kumar, S., 2014. Characteristics of air entrainment during dynamic wetting failure along a planar substrate. J. Fluid Mech. 747, 119–140.
Voinov, O.V., 1976. Hydrodynamics of wetting. Fluid Dyn. 11 (5), 714–721. doi:10.1007/bf01012963.
Weinstein, S.J., Ruschak, K.J., 2004. Coating flows. Annu. Rev. Fluid Mech. 36, 29–53.
Wu, J.-Z., Ma, H.-Y., Zhou, M.D., 2006. Vorticity and vortex dynamics. Springer.
Yarin, A.L., 2006. Drop impact dynamics: splashing, spreading, receding, bouncing. Annu. Rev. Fluid Mech. 38, 159–192. doi:10.1146/annurev.fluid.38.050304.092144.